SCIENCE CHINA
Information Sciences

• RESEARCH PAPER •

April 2026, Vol. 69, Iss. 4, 142403:1–142403:10
https://doi.org/10.1007/s11432-025-4643-6

Multimode-fused reservoir computing based on $CH_3NH_3PbI_3$ nanowire optoelectronic memristor for spatiotemporal information processing

Yue WANG[1], Xuanyu SHAN[1*], Qiang WANG[2], Zewei WANG[2], Siyu LIU[2], Wei LIU[1], Jiahui ZHENG[1], Xiaoning ZHAO[1*], Zhongqiang WANG[1*], Ya LIN[1], Ye TAO[1], Haiyang XU[1] & Yichun LIU[1]

[1]*State Key Laboratory of Integrated Optoelectronics, Northeast Normal University, Changchun 130024, China*
[2]*China FAW Group Co., Ltd., Changchun 130011, China*

Received 17 July 2025/Revised 10 September 2025/Accepted 21 October 2025/Published online 11 February 2026

Abstract Multiple sensing and processing capabilities enable an organism to obtain comprehensive information and make real-time decisions in unstructured environments. Inspired by the biological counterpart, developing neuromorphic hardware with multimodal fusion is supposed to realize high-precision processing for complex information. In this work, we developed a visual-auditory-fused reservoir computing system by combining a $CH_3NH_3PbI_3$ nanowire/pentacene optoelectronic memristor and a sound sensor. Under the stimulation of optical/electrical signals, the $CH_3NH_3PbI_3$ nanowire-based device exhibited volatility under optical or electrical stimulation, providing an essential foundation for visual-auditory-fused reservoir computing. The motion detection function was demonstrated using synchronous visual and auditory sensory information. Compared with single sensory input, the detection accuracy increased from 51.2% to 95.5% by combining the visual and auditory modalities. The results presented in this work provide a promising strategy to develop efficient multimodal neuromorphic hardware for human-robot interactions.

Keywords multisensory-fused, reservoir computing, optoelectronic memristor, halide perovskite, neuromorphic device

Citation Wang Y, Shan X Y, Wang Q, et al. Multimode-fused reservoir computing based on $CH_3NH_3PbI_3$ nanowire optoelectronic memristor for spatiotemporal information processing. Sci China Inf Sci, 2026, 69(4): 142403, https://doi.org/10.1007/s11432-025-4643-6

1 Introduction

Multisensory-fused perception is a crucial survival skill for organisms to achieve information acquisition and decision-making in unstructured, sophisticated environments [1–3]. Compared with single sensory inputs, the integration of multimodal information can effectively prevent inaccurate judgment induced by unreliable data [4–6]. For instance, visual information in an environment will enhance the auditory localization accuracy of sound sources to perceive danger in advance. Traditional artificial perception system usually integrates various sensors to obtain environmental stimuli carrying multimodal information, where single sensory input information is processed independently before data fusion [7, 8]. Herein, the dimension mismatch between different modalities imposes high demands on the computation and hardware of the system, resulting in increased energy consumption and data delay [9,10]. However, the physical separation of the sensing, storage, and processing units leads to frequent data transmissions, which is not beneficial for highly efficient perception [11,12]. Inspired by biological counterparts, developing a neuromorphic multimodal perception system with an in-sensor computing architecture provides an ideal platform to overcome the aforementioned bottleneck [13–15]. Recently, Ji et al. [16, 17] developed brain-inspired in-memory computing systems for video sentiment analysis and the recognition and imagination of multimodal information, which provides a promising solution for the construction of efficient neuromorphic perception systems.

Among the various primary sensory systems, visual perception accounts for more than 80% of the external information that human beings receive [18]. Optoelectronic memristors have attracted extensive attention in artificial visual systems owing to the multifunctional integration of optical response and neuromorphic computation [19, 20].

* Corresponding author (email: danxy453@nenu.edu.cn, zhaoxn430@nenu.edu.cn, wangzq752@nenu.edu.cn)

Furthermore, the internal dynamic process with multidimensional coordinated modulation provides an ideal platform for multimodal perception [21, 22]. For example, Tu et al. [23] proposed an artificial visual-tactile perception system based on the composite of mechanoluminescence (ZnS:Cu) and photostimulated luminescence (CaSrS:Eu). Herein, force-induced mechanical signals can be directly converted into photons and transmitted to the photoreceptor layer, which accurately identifies the material hardness and transparency. Han et al. [24] developed a neuromorphic visual system with humidity adaptability based on an MXene-ZnO memristor, in which the humidity-related image preprocessing function is demonstrated. The auditory sense is another crucial pathway for communication, promoting associative learning and memory in the human brain [25]. The visual-auditory-fused perception is a key approach for achieving efficient and low-energy perception in unstructured environments. When visual and auditory stimuli share complex and task-relevant features, perceptual and behavioral benefits are significantly enhanced. For example, multisensory integration areas, such as the posterior superior temporal cortex, exhibit reduced neural variability under noisy conditions, which enhances audiovisual speech perception accuracy [26, 27]. Therefore, visual-auditory-fused perception systems can advance the development of humanoid robots and autonomous driving technologies [28, 29]. Developing a novel high-performance memristive material is an essential foundation for efficient visual-auditory-fused perception.

Halide perovskites are considered ideal functional materials for optoelectronic devices owing to their high absorption coefficients, high carrier mobilities, and defect-tolerant properties [30, 31]. Furthermore, high-crystallized perovskite nanowires, compared with traditional films, exhibit outstanding optoelectronic performance, which can be attributed to their few grain boundaries and low defect concentration [32, 33]. High-performance photodetectors and solar cells have been developed using the excellent quantum efficiency of perovskite nanowires [34, 35]. Furthermore, neuromorphic devices based on perovskite nanowires have been constructed to implement spatiotemporal information processing. For instance, Long et al. [36] fabricated a spherical bionic eye based on metal-oxide nanotube/perovskite nanowires, providing a feasible strategy to demonstrate color vision and optical adaptivity. Benefiting from the remarkable advances of the perovskite nanowire-based devices, the coordinated modulation of internal dynamic processes through multidimensional signals lays the indispensable basis for efficient multimodal perception.

In this work, we demonstrate an optoelectronic memristor based on $CH_3NH_3PbI_3$ nanowires and an organic semiconductor (pentacene) heterojunction structure. These one-dimensional materials with a high specific surface area enable dynamic temporal responses. A variety of synaptic functions, including excitatory postsynaptic current (EPSC) and paired-pulse facilitation (PPF), have been emulated using photonic and electric stimulations. Furthermore, a multimodal reservoir computing system is developed to encode spatiotemporal information from visual and auditory sensory inputs, which enables highly efficient motion detection in complex environments. This study proposes a novel optoelectronic synaptic device with volatile memristive characteristics, which may provide a hardware foundation for neuromorphic multimodal perception systems.

2 Experimental

2.1 Materials

Lead iodide (PbI_2, Xi'an Yuri Solar Co., Ltd., 99.999%), methylammonium iodide (CH_3NH_3I, Xi'an Yuri Solar Co., Ltd., 99.5%), *N*, *N*-dimethylformamide (DMF, Macklin, 99.5%), isopropanol (IPA, Sinopharm Chemical Reagent Co., Ltd., 99.7%) and pentacene (Aladdin, 98%).

2.2 Preparation of precursor solutions

A $CH_3NH_3PbI_3$ precursor solution (1 mM) was prepared by dissolving 461 mg of PbI_2 and 159 mg of CH_3NH_3I in 1 mL of DMF at 85°C while stirring. The mixed solution was prepared by dissolving 200 μL of DMF in 3 mL of IPA at 80°C while stirring.

2.3 Fabrication of the device

First, indium tin oxide (ITO) on glass substrates (2.25 cm^2) was sequentially cleaned in trichloroethylene, acetone, ethanol, and deionized water. Second, the washed substrates were treated with ultraviolet ozone for 15 min. Finally, $CH_3NH_3PbI_3$ nanowires were fabricated through a two-step spin coating procedure. First, 80 μL of the $CH_3NH_3PbI_3$ precursor solution was added to the ITO substrate and sequentially spin-coated at 500 r/min for 5 s and at 3000 r/min for 30 s, followed by annealing on a hotplate at 70°C for 5 min. Subsequently, the mixed solution of 200 μL was deposited onto the annealed film and spin-coated at 3000 r/min for 30 s, followed by annealing on a

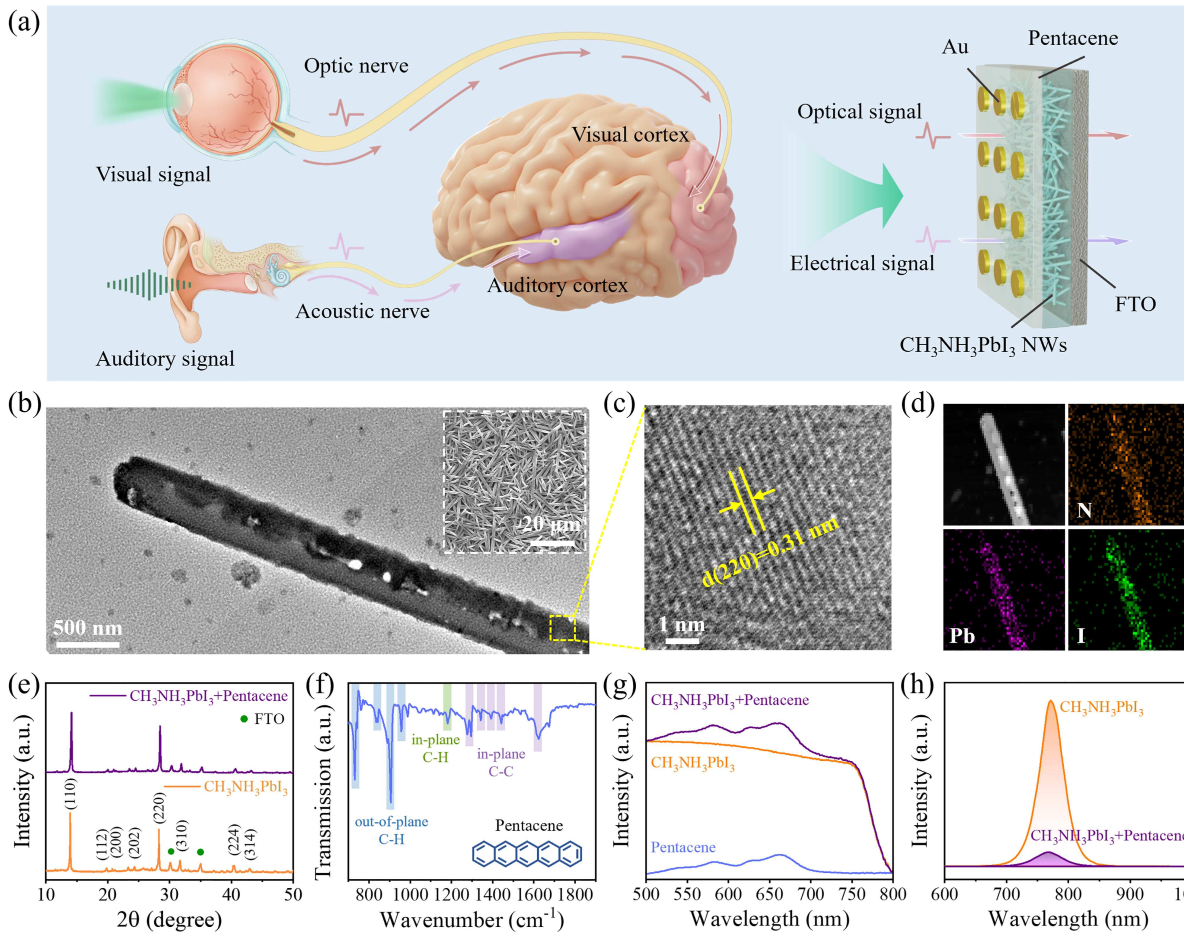

Figure 1 (Color online) Structure and characterization of the $CH_3NH_3PbI_3$ nanowire-based memristor. (a) Schematic of human visual and auditory sensory systems for acquiring external information, and a bionic $CH_3NH_3PbI_3$ nanowire-based memristor. (b) TEM images of the $CH_3NH_3PbI_3$ nanowires. The inset shows the SEM image of $CH_3NH_3PbI_3$ nanowires. (c) High-resolution transmission electron microscopy images of the $CH_3NH_3PbI_3$ nanowires. (d) Corresponding EDX spectra of N, Pb, and I elements. (e) X-ray diffraction images of $CH_3NH_3PbI_3$ nanowires and $CH_3NH_3PbI_3$ nanowires/pentacene film. (f) Fourier-transform infrared spectroscopy of pentacene thin films. (g) UV-visible absorption and (h) PL spectra of the $CH_3NH_3PbI_3$ nanowires, pentacene, and composite film.

100°C hotplate for 30 min to complete the preparation of the $CH_3NH_3PbI_3$ nanowire layer. Pentacene was thermally evaporated onto the $CH_3NH_3PbI_3$ nanowire layer under 3×10^{-4} Pa. Finally, an optoelectronic memristor was produced by depositing a 200 μm diameter Au top electrode using a shadow mask through thermal evaporation.

2.4 Characterization

Optical signals during the measurement were generated using a xenon lamp (LA-410UV, Hayashi). Memristive properties were measured using a semiconductor analyzer (2636B, Keithley) and probe station (TTPX, Lake Shore). Current flow from the top electrode (Au) to the bottom electrode (ITO) was defined as the positive direction. Pulse measurements were made using an arbitrary function generator (TGA12104) and oscilloscope (TPO70404C, Tektronix). All the measurements were performed under ambient atmospheric conditions.

3 Result and discussions

Figure 1(a) shows a schematic of the human visual and auditory systems, illustrating the motivation for constructing an optoelectronic memristor for multimodal perception systems. For the human visual system, the retina can filter out irrelevant information and enhance image features, i.e., the preprocessing function. Then, the preprocessed image information is transmitted to the visual cortex via the optic nerve for advanced processing [37,38]. In conjunction with the visual perception system, the auditory sensory system enables the detection of sound signals with different frequencies through the transduction pathway [39]. The eardrum generates mechanical vibrations upon receiving sound signals, which are converted into electrical signals owing to the fluid within the cochlea. The auditory cortex in the brain processes the impulse sequence and perceives it as sounds [40]. However, unavoidable ambiguities usually affect subsequent decision-making and appropriate responses owing to the unreliable information in single sensory input [41]. Therefore, developing an integrated multimodal fusion for accuracy perception is a feasible solution. In order to realize the visual-auditory-fused perception, we fabricated an optoelectronic memristor with the structure Au/Pentacene/$CH_3NH_3PbI_3$ nanowire layer/ITO. The $CH_3NH_3PbI_3$ nanowire films were synthesized through the dissolution-recrystallization process (Section 2, Figure S1) [42]. The pentacene layer, fabricated via vacuum evaporation, exhibits outstanding performance in optoelectronic devices, owing to its good crystallinity and excellent air stability. Simultaneously, as a hole transport layer with high hole mobility, it forms a heterojunction with $CH_3NH_3PbI_3$ nanowires, making it suitable for modulating carrier transport to emulate synaptic functions. A corresponding high-resolution transmission electron microscopy image of $CH_3NH_3PbI_3$ nanowires is shown in Figure 1(b). The as-synthesized nanowires exhibit a typical diameter of ~200 nm. The top-sectional SEM image illustrates that the uniform length of the nanowires is ~20 μm (inset in Figure 1(b)). The lattice fringe of 0.31 nm corresponds to the (220) plane of the tetragonal crystal structure, as shown in Figure 1(c) [42,43]. Furthermore, energy-dispersive spectrometer element mapping indicates the uniform distribution of N, Pb, and I (Figure 1(d)). The crystallinity of the $CH_3NH_3PbI_3$ nanowires is confirmed through X-ray diffraction, as shown in Figure 1(e). The $CH_3NH_3PbI_3$ nanowires tend to grow along the [110] direction, as indicated by the higher (110) and (220) diffraction peaks [44]. For the pentacene film, the Fourier-transform infrared (FTIR) results are plotted in Figure 1(f). The peaks at 730, 835, 906, 956, and 1182 cm^{-1} are assigned to the out-of-plane and in-plane C-H vibrations. Meanwhile, the vibrations at 1296, 1342, 1392, 1443, and 1623 cm^{-1} correspond to the in-plane C-C stretching modes [45, 46]. UV-visible absorption spectra of the $CH_3NH_3PbI_3$ nanowires, pentacene, and composite film are shown in Figure 1(g). The $CH_3NH_3PbI_3$ nanowire/pentacene nanocomposite film exhibits a wide absorption range centered at 750 nm. The wide absorption band is beneficial for visible perception. Compared with pure $CH_3NH_3PbI_3$ nanowires, the composite film achieves higher photogenerated carrier separation efficiency, which is evaluated through photoluminescence (PL) spectroscopy, as shown in Figure 1(h). The nanocomposite films exhibited a weaker emission peak at ~770 nm owing to the effective photogenerated exciton transference at the $CH_3NH_3PbI_3$ nanowires/pentacene interface.

In a biological system, information transmission between presynaptic and postsynaptic neurons relies on the neurotransmitters in the synaptic gaps [47]. The released neurotransmitter combines with the receptors in postsynaptic neurons, leading to the generation of postsynaptic current [48]. The potentiation and depression of a synaptic connection is called synaptic plasticity [49]. In this section, the basic synaptic characteristics are demonstrated through electrical stimulations. The I-V curve of the $CH_3NH_3PbI_3$ nanowires/pentacene memristor is shown in Figures 2(b) and (c). When applying a positive sweep (0 V $\rightarrow$ +2 V $\rightarrow$ 0 V) to the Au electrode, a gradual increase in current is observed. Conversely, the device current decreases gradually during the successive negative voltage sweeps. Herein, the device current is treated as a synaptic weight, which can be attributed to the electron trapping at the $CH_3NH_3PbI_3$ nanowire-pentacene interface. For comparison, the electrical measurement of the pure $CH_3NH_3PbI_3$ nanowire-based device is shown in Figure S2. The I-V curves under the voltage sweeps show negligible current enhancements, which is not beneficial for synaptic emulation. Figure 2(d) shows 10 cycles of potentiation (1.5 V, 1 μs, 50 pulses) and depression (−0.4 V, 1 μs, 50 pulses) behaviors under the electrical pulse mode. The switching operation exhibits negligible degradation, indicating excellent cycling stability. As shown in Figure 2(e), the cumulative distribution heatmap depicts the current variation (ΔI) versus the device current (I) during potentiation and depotentiation. The results confirm the satisfactory device stability and reproducibility of the developed $CH_3NH_3PbI_3$ nanowire/pentacene-based memristor. Furthermore, the current changes, dependent on the pulse duration, time interval, and amplitude, are plotted in Figure 2(f). As shown, a larger current change could be obtained under the electrical stimulation of longer duration, shorter time interval, and higher amplitude, which are consistent with the behavior of biological synapses [50].

In addition to the electrical memristive behavior, the optoelectronic response of the proposed device has also been investigated, as shown in Figure 3(a). The optoelectronic memristor was irradiated with optical signals of 320, 532, and 640 nm. The optical intensity was fixed at 0.22 mW/cm^2, and the photocurrent evolution was monitored by applying a bias voltage of 0.1 V. Corresponding photoresponse curves under different wavelengths are shown in Figure 3(b). The device exhibits an increased photocurrent after the light is turned on, which resembles the learning process. When the light is switched off, a spontaneous photocurrent decay is obtained, i.e., forgetting process [51]. In contrast, the pure $CH_3NH_3PbI_3$-based device exhibits volatile photoresponse behavior, as shown in Figure S3. Among them, the optical signal of 532 nm induces the highest response amplitude, which is consistent with the absorption spectra shown in Figure 1(g). The optical signal of 532 nm was selected for the subsequent optoelectronic memristive measurements. Finally, the effects of light intensity, duration, and frequency on synaptic weight were

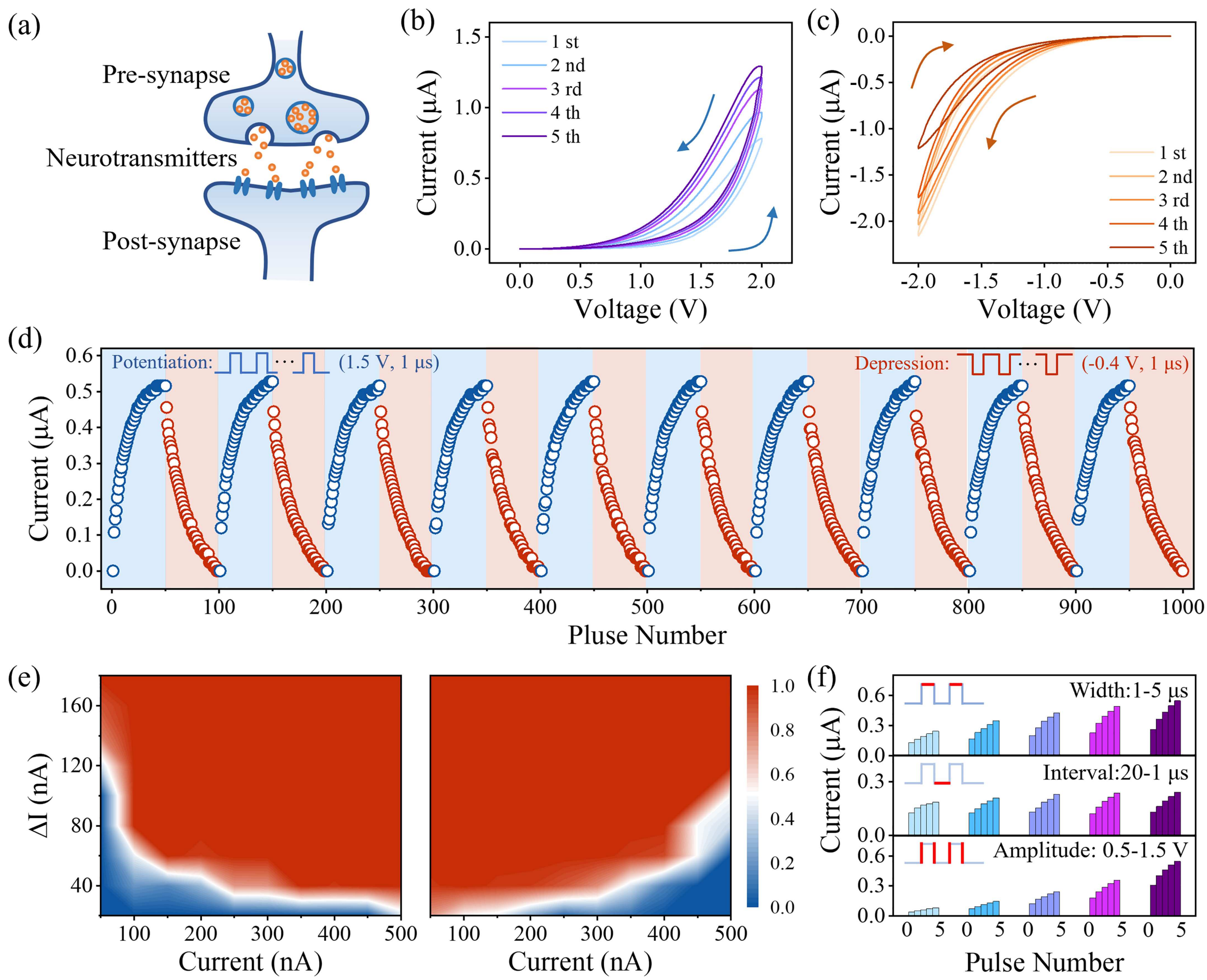

Figure 2 (Color online) Electrical performances of the $CH_3NH_3PbI_3$ nanowires/pentacene memristor. (a) Schematic of a biological synaptic. I-V curves of $CH_3NH_3PbI_3$ nanowires/pentacene memristor under consecutive (b) positive sweeping voltage and (c) negative sweeping voltage. (d) Cyclic electrical potentiation and depression behaviors. (e) Cumulative distribution function heatmap of the current variation (ΔI) versus current (I) statistical analysis of the $CH_3NH_3PbI_3$ nanowires/pentacene memristor during potentiation (left) and depression (right). (f) Current change of the $CH_3NH_3PbI_3$ nanowires/pentacene-based memristor at different voltage pulse durations, time intervals, and amplitudes.

investigated. Figure 3(c) shows the photocurrent response under various optical intensities (0.05, 0.29, 0.54, 0.95, and 1.64 mW/cm^2) with a fixed duration of 1 s. It is evident that the photocurrent increases with the increased optical intensity, which is related to the trapping of photogenerated carriers at the $CH_3NH_3PbI_3$ nanowire/pentacene interfaces. Figure 3(d) presents the impact of light duration (0.5, 1, 2, 3, and 5 s) on photocurrent. A longer duration results in a higher photocurrent and a longer relaxation process, which is similar to the transition from short-term memory to long-term memory [52]. Then, the synaptic function of PPF is emulated by applying a pair of pulses with various time intervals (Δt) [53]. The photocurrent activated by the second pulse (A_2) is higher than that activated by the first one (A_1). Figure 3(e) shows the PPF index (A_2/A_1) dependent on Δt between two successive pulses. The PPF index decreases gradually as Δt increases, which can be fitted with an exponential function. Additionally, the optoelectronic memristor also exhibits plasticity that is dependent on frequency and pulse number, as presented in Figures 3(f) and (g). The EPSC level and relaxation time gradually increased with the increase in the pulse frequency and pulse number.

Moreover, the "learning-experience" behaviors were emulated, in which the learning and forgetting processes correspond to the illumination and darkness, respectively [54]. For the first learning-forgetting process, the synaptic weights were potentiated upon optical stimulation (40 pulses) and then decayed into an intermediate state spontaneously after the optical stimulation was removed (Figure S4). With regard to the relearning process, a relearning process of only 13 pulses was sufficient to recover the memory decay. After the same forgetting process of 15 s, the memory retention ratio increased from 44.7% to 51.4%. Furthermore, the international Morse codes were used to

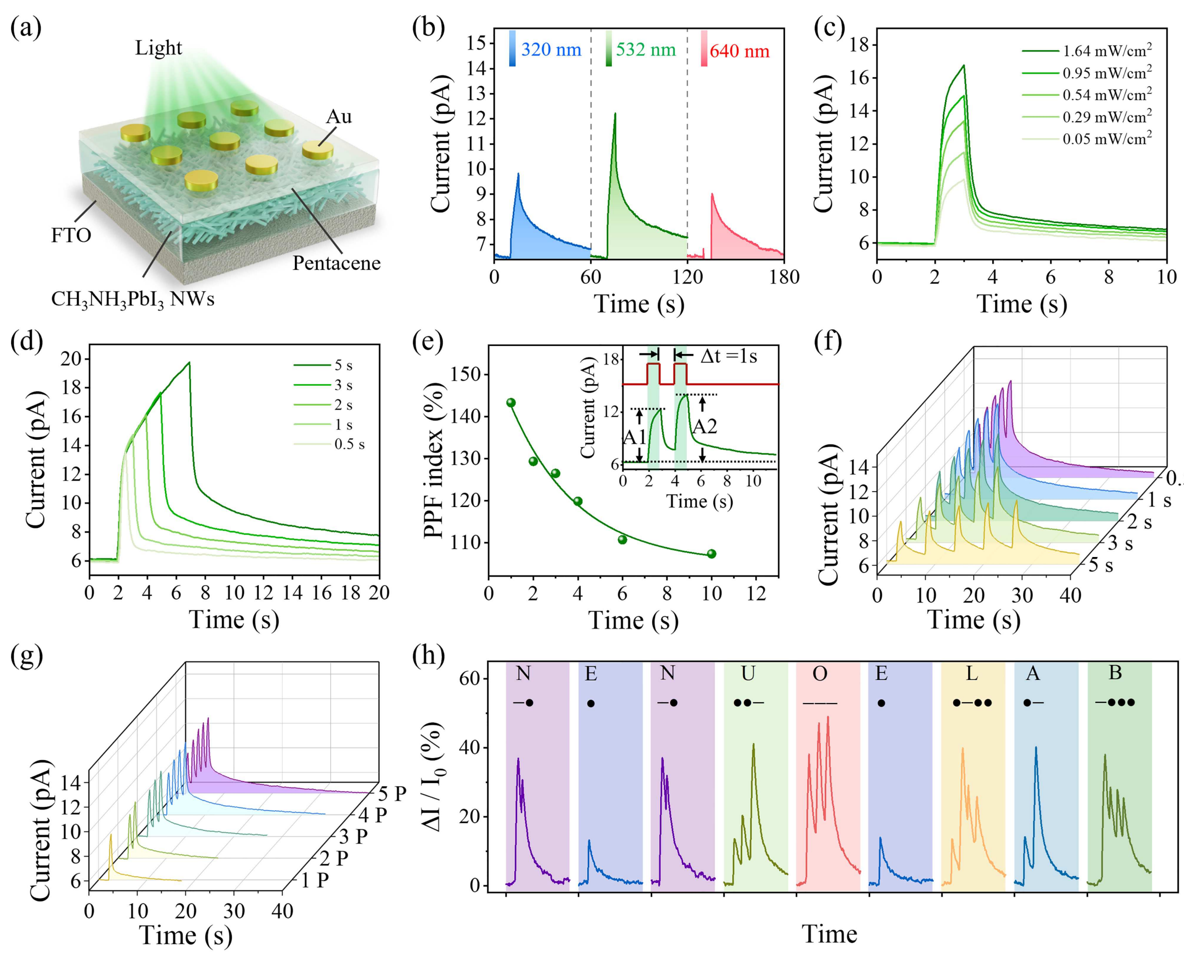

Figure 3 (Color online) Optoelectronic memristive behaviors of the $CH_3NH_3PbI_3$ nanowire/pentacene memristor. (a) Schematic of optoelectronic measurement under visible light. (b) Photocurrent induced by red, green, and blue pulses. (c) Photocurrent enhancement of the developed device under a single optical pulse with various intensities (0.05, 0.29, 0.54, 0.95, and 1.64 mW/cm^2). (d) Photocurrent enhancement under the optical pulse with various durations (0.5, 1, 2, 3, and 5 s). (e) PPF index dependent on the time interval. Inset: a typical PPF curve with 1 s intervals. The optical synaptic plasticity correlation with (f) the frequency of pulses and (g) the number of pulses. (h) A series of photonic pulses with the international Morse code of "NENUOELAB".

pattern photonic signals, to investigate the ability for optical information processing [55]. Herein, the dot and dash were encoded by optical pulses with durations of 100 and 400 ms, respectively, while the time interval was fixed at 500 ms. As shown in Figure 3(h), each letter induced a distinct photoresponse amplitude, which combined to form the word "NENUOELAB". These results demonstrate the potential of our device for optical wireless communication in human-machine interfaces.

The underlying mechanism of our $CH_3NH_3PbI_3$ nanowire-based optoelectronic memristor was also investigated. As shown in Figure 4(a), an in-situ X-ray photoelectron spectroscopy analysis is performed to determine the interval energy level alignment. The optical signals of 532 nm are selected for in situ illumination. Compared with pure $CH_3NH_3PbI_3$ nanowires, the Pb 4f and I 3d peaks shift toward lower binding energies by 0.3 and 0.4 eV, respectively, which confirms the holes transfer from $CH_3NH_3PbI_3$ nanowires to pentacene in the initial dark state. After optical irradiation, the characteristic peaks of the $CH_3NH_3PbI_3$ nanowires further shifted toward lower binding energy (0.2 eV), indicating the effective transfer of photogenerated holes from $CH_3NH_3PbI_3$ nanowires to pentacene [56, 57]. A general model is proposed to explain the optoelectronic memristive process, as shown in Figures 4(d)–(f). The optical stimulation excited the electrons to the conduction band, resulting in photogenerated holes in the valence band of $CH_3NH_3PbI_3$ nanowires. This process corresponds to the increased device current. Part of the photogenerated holes will transfer to the pentacene layer, corresponding to the nonvolatile photoresponse. When the light is off, the trapped holes are released into $CH_3NH_3PbI_3$ and subsequently recombine with electrons.

In biological systems, the integration of multisensory information can efficiently prevent misjudgment in complex environments induced by unreliable data [6, 58]. For instance, motion detection in the visual system can be achieved by comparing the target locations at different moments. However, the complicated external environment may in-

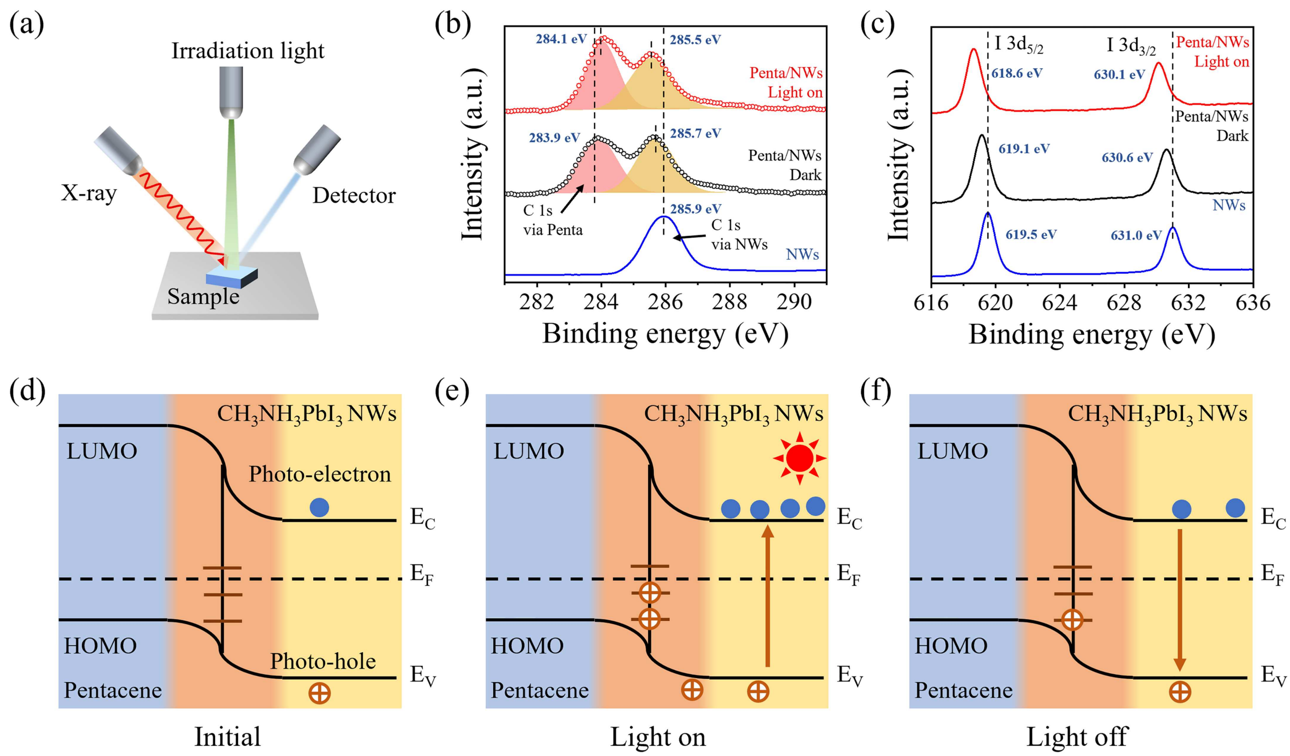

Figure 4 (Color online) (a) Schematic of in-situ XPS characterizations. High-resolution XPS spectra of (b) C 1s and (c) I 3d of $CH_3NH_3PbI_3$ nanowires and pentacene/$CH_3NH_3PbI_3$ nanowires under dark and light irradiation. Schematic diagrams of the band diagram at the pentacene/$CH_3NH_3PbI_3$ nanowire film interface, (d) in the initial state, (e) under visible irradiation, and (f) when the light is removed.

fluence the reliability of image information, such as undesired ambient occlusion or shadows. Accuracy judgment is supposed to be achieved by combining synchronous information from another sensory modality. In this section, the visual-auditory-fused perception function is demonstrated by combining our optoelectronic memristor with a sound sensor. An optoelectronic memristor array with 20 × 20 pixels was constructed to encode spatiotemporal visual information to perceive dynamic motion. As shown in Figure 5(b), four consecutive image frames at different moments are detected using our optoelectronic memristive array. The photocurrent in each pixel will decay spontaneously when the target object (cat) moves. The superposition of the obtained frames allows the integration of the spatiotemporal motion information, in which the statistical pixel output is indispensable for motion detection. For the lying down state, the cat almost remains static, and the imaged pixels receive a 4-bit pulse sequence of "1111" for subsequent reservoir computing. Conversely, the moving cat can result in the imaged pixels moving to different locations. The corresponding detection results for three typical behaviors (running, lying down, and playing) of the cat are plotted in Figure 5(c), which exhibits an obvious difference in the output amplitude distribution. In addition to the visual perception system, the auditory system offers more necessary information for high-precision status judgment. For example, the bell sound can efficiently prove the motion state of the cat, even in the blind areas. Figure 5(d) demonstrates the bell sounds of three different states for the cat. Here, a sound sensor array is connected to the optoelectronic memristor, which converts sound into electrical signals, as shown in Figure 5(e). The dependence of the response amplitude on sound intensity is shown in the right panel of Figure S7. Then, the multimodal synchronized perception is demonstrated using the internal dynamic process of the proposed optoelectronic device. The current output induced by optical and auditory signals is shown in Figure 5(f). The coexistence of optical and auditory signals considerably improves the current amplitude, which influences the statistical results for multimodal motion detection (Figure 5(g)). For instance, the reservoir states induced by the combined signal sequence "0001" are even higher than those induced by a single optical or auditory signal or with the sequence "1111". The normalized output threshold of the optoelectronic fusion mode is selected to distinguish the moving and static states. The corresponding static results for singular and multimodal inputs are plotted in Figure 5(h). The result shows that the visual-auditory-fused mode realizes a higher recognition rate (95.5%) than the singular visual (51.2%) or auditory mode (93.3%), indicating higher decision-making accuracy for complex environments.

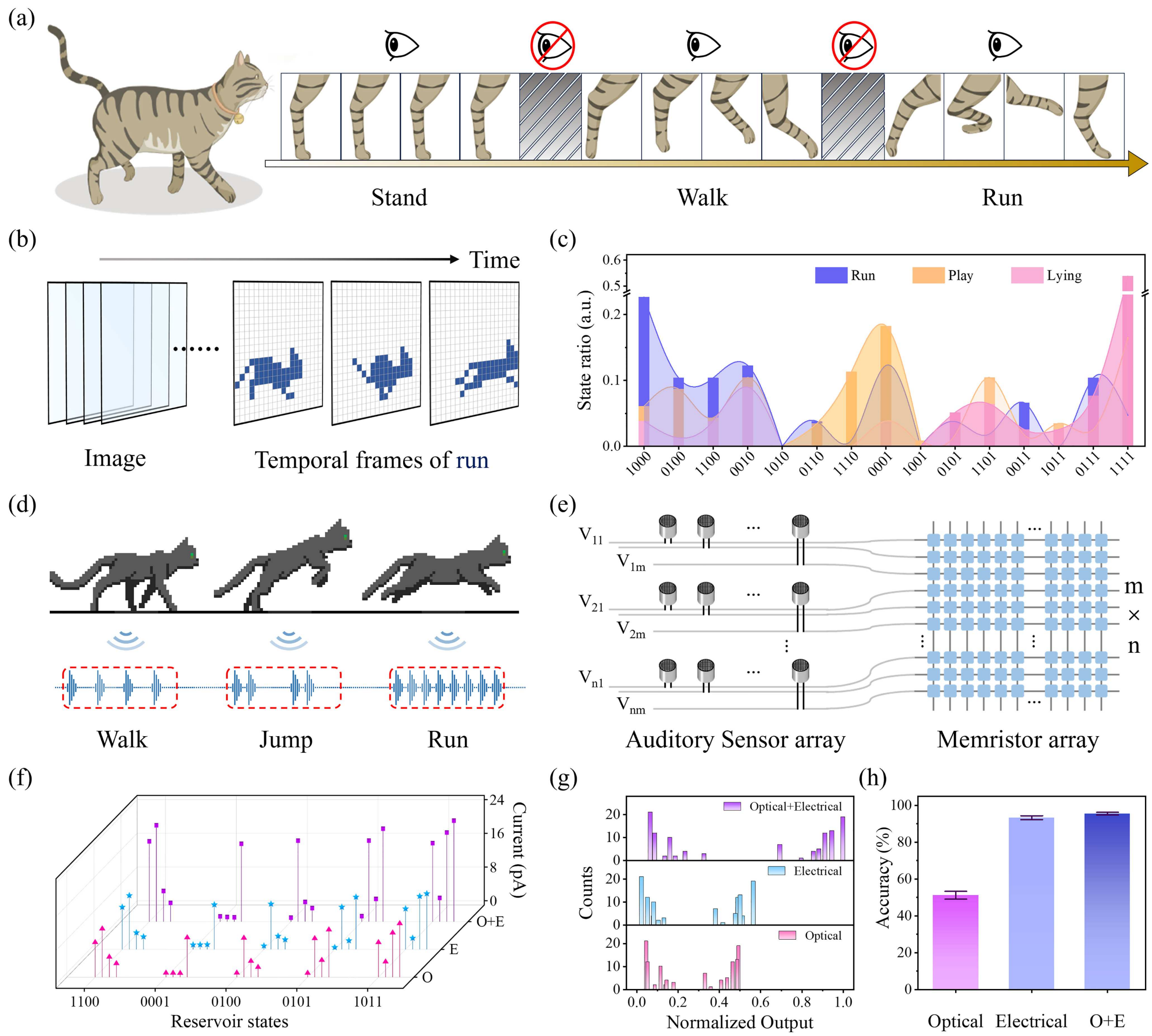

Figure 5 (Color online) Multimode reservoir computing for optoelectronic signal processing. (a) Schematic of the cat's behavior in different postures. (b) Visualization of the motion in a sequence of four frames (T1 + Δt). The pixels in a specific column of the temporal frames form the temporal vision sequence. (c) Reservoir states ratio of three behaviors: "running", "lying", and "playing". (d) Three typical audio patterns, namely "jump", "walk", and "run". (e) Schematic circuit diagram of the auditory sensor and memristor array. (f) Current responses in three modes (optical, electrical, and optoelectronic fusion) by several input signals: (1100), (0001), (0100), (0101), and (1011). (g) Distribution of 4-bit reservoir states in three modes. (h) Accuracies obtained from the training in three modes.

4 Conclusion

In this study, a visual-auditory-fused reservoir computing system for motion detection, which comprises a CH_3NH_3-PbI_3 nanowire-based memristor and sound detector, was developed. Herein, the optoelectronic memristor exhibited volatile synaptic behaviors under the stimulation of optical and electrical signals, which can be attributed to the carriers trapped at the $CH_3NH_3PbI_3$/pentacene interface. Furthermore, multimodal motion detection was demonstrated using the synchronous information of visual and auditory modalities. The spatiotemporal information of a moving target was encoded for reservoir computing. Compared with single sensory inputs, the vision-auditory fusion can considerably enhance the detection accuracy, which increases from 51.2% to 95.5%. Our work provides a promising hardware foundation for highly efficient wireless communication toward real-time human-machine interaction.

Acknowledgements This work was supported by National Natural Science Foundation of China for Distinguished Young Scholars (Grant No. 52025022), Funds from Jilin Province (Grant No. 20240210002GX), National Natural Science Foundation of China (Grant Nos. U23A20568, 52372137, 52272140, 52402175, 52472149), China Postdoctoral Science Foundation (Grant No. GZB20240135), "111" Project (Grant No. B25030), Fundamental Research Funds for the Central Universities (Grant No. 2412024Q17006), and Scientific Research Innovation Capability Support Project for Young Faculty (Grant No. ZYGXQNJSKYCXNLZCXM-I10).

Supporting information Figures S1–S7. The supporting information is available online at info.scichina.com and link.springer.com. The supporting materials are published as submitted, without typesetting or editing. The responsibility for scientific accuracy and content remains entirely with the authors.

References

1 Duan S, Shi Q, Wu J. Multimodal sensors and ML-based data fusion for advanced robots. Adv Intell Syst, 2022, 4: 2200213
2 Tan H, Zhou Y, Tao Q, et al. Bioinspired multisensory neural network with crossmodal integration and recognition. Nat Commun, 2021, 12: 1120
3 Jung Y H, Park B, Kim J U, et al. Bioinspired electronics for artificial sensory systems. Adv Mater, 2019, 31: 1803637
4 Duan Q, Zhang T, Liu C, et al. Artificial multisensory neurons with fused haptic and temperature perception for multimodal in-sensor computing. Adv Intell Syst, 2022, 4: 2200039
5 Zhu J, Zhang X, Wang R, et al. A heterogeneously integrated spiking neuron array for multimode-fused perception and object classification. Adv Mater, 2022, 34: 2200481
6 Franzen L, Delis I, de Sousa G, et al. Auditory information enhances post-sensory visual evidence during rapid multisensory decision-making. Nat Commun, 2020, 11: 5440
7 Wang Y, Cai Y, Wang F, et al. A three-dimensional neuromorphic photosensor array for nonvolatile in-sensor computing. Nano Lett, 2023, 23: 4524–4532
8 Wang T Y, Meng J L, Li Q X, et al. Reconfigurable optoelectronic memristor for in-sensor computing applications. Nano Energy, 2021, 89: 106291
9 Yang C, Wang H, Zhou G, et al. A multimodal perception-enabled flexible memristor with combined sensing-storage-memory functions for enhanced artificial injury recognition. Small, 2024, 20: 2402588
10 Zhao L C, Zou H X, Wei K X, et al. Mechanical intelligent energy harvesting: from methodology to applications. Adv Energy Mater, 2023, 13: 2300557
11 Yu J, Wang Y, Qin S, et al. Bioinspired interactive neuromorphic devices. Mater Today, 2022, 60: 158–182
12 Midya R, Wang Z, Asapu S, et al. Reservoir computing using diffusive memristors. Adv Intell Syst, 2019, 1: 1900084
13 Fang H, Ma S, Wang J, et al. Multimodal in-sensor computing implemented by easily-fabricated oxide-heterojunction optoelectronic synapses. Adv Funct Mater, 2024, 34: 2409045
14 Ma S, Zhou Y, Wan T, et al. Bioinspired in-sensor multimodal fusion for enhanced spatial and spatiotemporal association. Nano Lett, 2024, 24: 7091–7099
15 Sun L, Wang Z, Jiang J, et al. In-sensor reservoir computing for language learning via two-dimensional memristors. Sci Adv, 2021, 7: eabg1455
16 Ji X, Dong Z, Han Y, et al. A brain-inspired hierarchical interactive in-memory computing system and its application in video sentiment analysis. IEEE Trans Circ Syst Video Technol, 2023, 33: 7928–7942
17 Ji X, Dong Z, Lai C S, et al. A brain-inspired in-memory computing system for neuronal communication via memristive circuits. IEEE Commun Mag, 2022, 60: 100–106
18 Wang G, Wang R, Kong W, et al. Simulation of retinal ganglion cell response using fast independent component analysis. Cogn Neurodyn, 2018, 12: 615–624
19 Yan X, He H, Liu G, et al. A robust memristor based on epitaxial vertically aligned nanostructured $BaTiO_3$-CeO_2 films on silicon. Adv Mater, 2022, 34: 2110343
20 Gao S, Liu G, Yang H, et al. An oxide Schottky junction artificial optoelectronic synapse. ACS Nano, 2019, 13: 2634–2642
21 Pan X, Wang J, Deng Z, et al. A memristor-based bioinspired multimodal sensory memory system for sensory adaptation of robots. Adv Intell Syst, 2022, 4: 2200031
22 Yan X, Zhang Y, Fang Z, et al. A multimode-fused sensory memory system based on a robust self-assembly nanoscaffolded $BaTiO_3$:Eu_2O_3 memristor. InfoMat, 2023, 5: e12429
23 Guo J, Guo F, Zhao H, et al. In-sensor computing with visual-tactile perception enabled by mechano-optical artificial synapse. Adv Mater, 2025, 37: 2419405
24 Wang Y, Gong Y, Yang L, et al. MXene-ZnO memristor for multimodal in-sensor computing. Adv Funct Mater, 2021, 31: 2100144
25 Kolarik A J, Moore B C J, Zahorik P, et al. Auditory distance perception in humans: a review of cues, development, neuronal bases, and effects of sensory loss. Atten Percept Psychophys, 2016, 78: 373–395
26 Opoku-Baah C, Schoenhaut A M, Vassall S G, et al. Visual influences on auditory behavioral, neural, and perceptual processes: a review. J Assoc Res Oto, 2021, 22: 365–386
27 Ozker M, Schepers I M, Magnotti J F, et al. A double dissociation between anterior and posterior superior temporal gyrus for processing audiovisual speech demonstrated by electrocorticography. J Cogn Neurosci, 2017, 29: 1044–1060
28 Bednarek M, Kicki P, Walas K. On robustness of multi-modal fusion-robotics perspective. Electronics, 2020, 9: 1152
29 Song Y, Li Z, Li G, et al. Multi-sensory visual-auditory fusion of wearable navigation assistance for people with impaired vision. IEEE Trans Automat Sci Eng, 2025, 22: 4724–4736
30 Chen Q, De Marco N, Yang Y M, et al. Under the spotlight: the organic-inorganic hybrid halide perovskite for optoelectronic applications. Nano Today, 2015, 10: 355–396
31 Liu L, Ma Y, Wang Y, et al. Hole-transport management enables 23%-efficient and stable inverted perovskite solar cells with 84% fill factor. Nano-Micro Lett, 2023, 15: 117
32 Wu D, Xu Y, Zhou H, et al. Ultrasensitive, flexible perovskite nanowire photodetectors with long-term stability exceeding 5000 h. InfoMat, 2022, 4: e12320
33 Zhang Y, Ma Z, Chen Z, et al. Perovskite-nanowire-array-based continuous-state programmable artificial synapse for neuromorphic computing. Adv Intell Syst, 2024, 6: 2300586
34 Feng J, Gong C, Gao H, et al. Single-crystalline layered metal-halide perovskite nanowires for ultrasensitive photodetectors. Nat Electron, 2018, 1: 404–410
35 Im J H, Luo J, Franckevičius M, et al. Nanowire perovskite solar cell. Nano Lett, 2015, 15: 2120–2126
36 Long Z, Qiu X, Chan C L J, et al. A neuromorphic bionic eye with filter-free color vision using hemispherical perovskite nanowire array retina. Nat Commun, 2023, 14: 1972
37 Wan C, Cai P, Wang M, et al. Artificial sensory memory. Adv Mater, 2020, 32: 1902434
38 Choi C, Choi M K, Liu S, et al. Human eye-inspired soft optoelectronic device using high-density MoS_2-graphene curved image sensor array. Nat Commun, 2017, 8: 1664
39 Hudspeth A J. Integrating the active process of hair cells with cochlear function. Nat Rev Neurosci, 2014, 15: 600–614
40 Dalhoff E, Turcanu D, Zenner H P, et al. Distortion product otoacoustic emissions measured as vibration on the eardrum of human subjects. Proc Natl Acad Sci USA, 2007, 104: 1546–1551
41 Green A M, Angelaki D E. Multisensory integration: resolving sensory ambiguities to build novel representations. Curr Opin Neurobiol, 2010, 20: 353–360
42 Zhu P, Gu S, Shen X, et al. Direct conversion of perovskite thin films into nanowires with kinetic control for flexible optoelectronic devices. Nano Lett, 2016, 16: 871–876

43 Gao L, Zeng K, Guo J, et al. Passivated single-crystalline $CH_3NH_3PbI_3$ nanowire photodetector with high detectivity and polarization sensitivity. Nano Lett, 2016, 16: 7446–7454

44 Liu M, Johnston M B, Snaith H J. Efficient planar heterojunction perovskite solar cells by vapour deposition. Nature, 2013, 501: 395–398

45 Frątczak E Z, Uznański P, Moneta M E. Characterization of molecular organization in pentacene thin films on SiO_2 surface using infrared spectroscopy, spectroscopic ellipsometry, and atomic force microscopy. Chem Phys, 2015, 456: 49–56

46 Hudgins D M, Allamandola L J. Infrared spectroscopy of matrix-isolated polycyclic aromatic hydrocarbon cations. 3. the polyacenes anthracene, tetracene, and pentacene. J Phys Chem, 1995, 99: 8978–8986

47 Mori M, Abegg M H, Gähwiler B H, et al. A frequency-dependent switch from inhibition to excitation in a hippocampal unitary circuit. Nature, 2004, 431: 453–456

48 Adermark L, Lovinger D M. Retrograde endocannabinoid signaling at striatal synapses requires a regulated postsynaptic release step. Proc Natl Acad Sci USA, 2007, 104: 20564–20569

49 McDonald J J, Teder-Sälejärvi W A, Ward L M. Multisensory integration and crossmodal attention effects in the human brain. Science, 2001, 292: 1791

50 Liu Q, Yin L, Zhao C, et al. Hybrid mixed-dimensional perovskite/metal-oxide heterojunction for all-in-one opto-electric artificial synapse and retinal-neuromorphic system. Nano Energy, 2022, 102: 107686

51 Shan X, Zhao C, Lin Y, et al. Optoelectronic synaptic device based on ZnO/HfO_x heterojunction for high-performance neuromorphic vision system. Appl Phys Lett, 2022, 121: 263501

52 Lee M, Lee W, Choi S, et al. Brain-inspired photonic neuromorphic devices using photodynamic amorphous oxide semiconductors and their persistent photoconductivity. Adv Mater, 2017, 29: 1700951

53 Lin Y, Zeng T, Xu H, et al. Transferable and flexible artificial memristive synapse based on WO_x Schottky junction on arbitrary substrates. Adv Elect Mater, 2018, 4: 1800373

54 Wang Z Q, Xu H Y, Li X H, et al. Synaptic learning and memory functions achieved using oxygen ion migration/diffusion in an amorphous InGaZnO memristor. Adv Funct Mater, 2012, 22: 2759–2765

55 Lee Y, Oh J Y, Xu W, et al. Stretchable organic optoelectronic sensorimotor synapse. Sci Adv, 2018, 4: eaat7387

56 Ji G, Zhao B, Song F, et al. The energy level alignment at the $CH_3NH_3PbI_3$/pentacene interface. Appl Surf Sci, 2017, 393: 417–421

57 Wang Y, Liu M, Fan F, et al. Enhanced full-spectrum photocatalytic activity of 3D carbon-coated C_3N_4 nanowires via giant interfacial electric field. Appl Catal B-Environ, 2022, 318: 121829

58 Bizley J K, Jones G P, Town S M. Where are multisensory signals combined for perceptual decision-making? Curr Opin Neurobiol, 2016, 40: 31–37